

Microstructural Characterization of a Double-Sided Friction Stir Weld on a Superaustenitic Stainless Steel

The formation of different microstructural zones in friction stir welded AL-6XN is described using results from various characterization techniques

BY S. KLINGENSMITH, J. N. DUPONT, AND A. R. MARDER

ABSTRACT. The microstructure of AL-6XN plates joined via a double-sided friction stir weld has been investigated. The microstructural zones that develop during friction stir welding (FSW) reflect decreasing strains and less severe thermal cycles with increasing distance from the weld centerline. The nugget, located around the centerline, has a refined structure of equiaxed grains as a result of the extreme strain and temperatures experienced during welding. Several features are seen within the nugget, one of the most prominent being a steady stream of tungsten inclusions created by accelerated tool wear. The heat-affected zone consists of a mixture of relatively large austenite grains and smaller recrystallized grains present at grain boundaries. These fine grains were shown to be austenite and no evidence of sigma phase in this region was apparent. The thermal mechanical-affected zone, located between the nugget and heat-affected zone, shows a microstructural transition from the completely refined structure to a structure very similar to the base metal. Of particular importance is that, unlike fusion welding, microsegregation has been avoided during FSW. Due to the changing microstructure from base metal to the weld zone, there are corresponding changes in hardness. Moving toward the centerline from the base metal, hardness increases due to refinement of the microstructure.

Introduction

Friction stir welding (FSW), which was developed by The Welding Institute (TWI) in 1991 (Ref. 1), is a solid-state welding process that offers an attractive alternative to fusion welding. The entire process appears relatively simple in that a

rotating tool is plunged between the surfaces of two abutting plates and is then traversed along the length of the plates. The advancing and retreating sides of the weld are defined by the direction of tool rotation with respect to the tool translation. On the advancing side, the tool rotation and translation are in the same relative direction while tool rotation and weld direction oppose each other at the retreating side. The tool consists of a shoulder that rotates against the plate surface and a pin that rotates beneath the plate surfaces. During the FSW process, frictional forces between the tool and plates create intense local heating. Instead of melting, a highly plasticized region of material around the rotating tool is created (Ref. 2). Material flow during FSW is very complex, but can be explained as a simple extrusion process. Tool rotation causes material transfer around the tool, stirring the two plates together. As the tool is translated, it essentially extrudes the stirred material through a "die" created by the tool and the unsoftened plate material (Refs. 3–6).

Although a number of materials have been joined via FSW, aluminum is the most commonly welded. Research has been performed on similar and dissimilar welds of aluminum alloys of the 1xxx, 2xxx, 5xxx, 6xxx, and 7xxx series (Refs. 2–5, 7–9). Microstructural zones that develop in heat-treatable aluminum alloys are similar and have been characterized extensively in the literature (Refs. 2–5, 7–10). Recently, there has been increasing interest in FSW of higher temperature materials such as

stainless steels. Although most stainless steels are readily weldable using standard welding techniques, FSW offers a number of advantages over fusion welding. Some benefits such as lower distortion, lower shrinkage, and elimination of porosity are a direct result of the lower operating temperatures and solid-state nature of FSW (Ref. 11). For stainless steels, two advantages make FSW particularly desirable. First, hexavalent chromium, a carcinogenic gas generated in arc welding by evaporation from the liquid pool and molten metal droplets (in consumable electrode processes), is absent in FSW (Ref. 12). Second, and most importantly, solidification defects commonly seen in fusion welding such as microsegregation can be avoided (Ref. 13). Microsegregation, resulting in Mo-depleted dendrite cores, is highly detrimental to the corrosion resistance of fusion welds and limits weld lifetime (Refs. 14–16). Despite these advantages, progress in FSW of higher temperature materials has been slow. Higher temperature materials like stainless steels are harder than aluminum alloys and have a higher flow stress. This harsh tool environment causes accelerated tool wear (Ref. 17), which ultimately limits process productivity and may also result in contamination of the weld zone. With proper tool design and better selection of tool material, however, wear can be minimized (Ref. 18).

Reynolds et al. (Ref. 19) has recently reported on the friction stir welding of a superaustenitic stainless steel (AL-6XN). These results showed that the base metal consisted of large equiaxed austenite grains with the sigma phase at the centerline. Similar to all other FS welds, the nugget consisted of refined grains, but no "onion rings" were observed. Surrounding the nugget, in the heat-affected zone (HAZ), a region of large austenite grains was observed with some type of phase with a small grain size at the grain boundaries.

KEYWORDS

AL-6XN Stainless Steel
Friction Stir Welding
Heat-Affected Zone (HAZ)
Superaustenitic Stainless Steel
Thermal Mechanical-Affected Zone (TMAZ)

S. KLINGENSMITH, J. N. DUPONT, and A. R. MARDER are with the Department of Materials Science and Engineering, Lehigh University, Bethlehem, Pa.

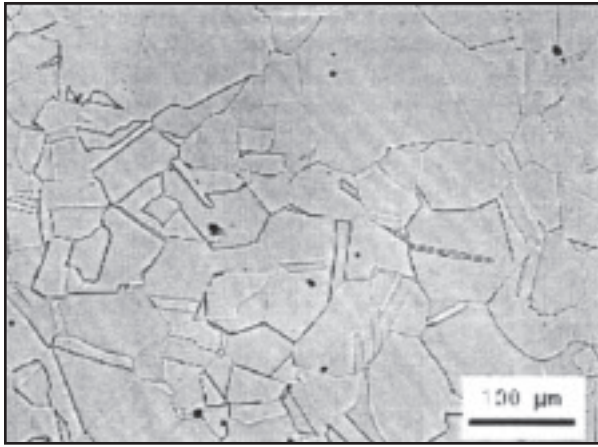


Fig. 1 — Base metal microstructure, which consists of large equiaxed austenite grains with annealing twins.

It was suggested that the smaller grains at grain boundaries were either the sigma phase or new, recrystallized austenite grains (Ref. 19). No detailed characterization was conducted to investigate this phenomenon. Although chemical nonhomogeneities (e.g., microsegregation) in FS welds are not expected due to the solid-state nature of the process, this has not been confirmed for FS welds produced on stainless steels. Thus, the objective of the present investigation is to provide a comprehensive microstructural characterization of a double-sided friction stir weld on AL-6XN.

Experimental Procedure

Two plates of AL-6XN were joined via a double-sided FS weld in a groove weld in a butt joint configuration. The plate thickness was 6.35 mm (0.25 in.). Welds were produced with a proprietary tungsten-based tool using a travel speed of approximately 0.847 mm/s (2 in./min), a tool rotational speed of 150 rpm, and a z-axis load of approximately 80 kN (18000 lb_f).

Cross sections of the transverse view of the welds were cut and prepared for microstructural analysis. Samples were mounted in a thermosetting epoxy and prepared according to standard metallographic preparation techniques. Samples were then electrolytically etched in a 10% oxalic acid solution and analyzed using light optical microscopy (LOM) and scanning electron microscopy (SEM). SEM was conducted on JEOL 6300 and XL30 microscopes. Grain size measurements were performed in selected areas according to ASTM E112 (Ref. 20). Four microhardness traces across the welds were performed with a LECO M400FT hardness tester in accordance with ASTM E384 (Ref. 21) using a load of 300 gm.

Characterization of the elemental distribution across different regions of the weld

was performed using electron probe microanalysis (EPMA). Regions of interest were marked and the samples were analyzed in the as-polished condition to avoid any surface relief from etching. EPMA was conducted using a JEOL 733 Superprobe equipped with four independent wavelength dispersive spectrometers. The analysis was completed using an accelerating voltage of 15 kV and a beam current of 32 nA. The $K\alpha$ lines were used for elements Fe, Ni, and Cr, while the $L\alpha$ line was used for Mo (Ref. 22). Raw data were converted to weight percentages using an established ZAF algorithm (Ref. 23). The base metal and weld zone were probed randomly to acquire representative compositions while four line scans were performed to check for composition changes across various regions of the weld. Two scans traversed from the first weld pass to the second weld pass, while two other line scans traversed from the weld zone into the base metal. Data were acquired at 10- μ m increments along lines that were approximately 500 μ m in length.

In addition, thin specimens approximately 20 \times 10 mm were extracted

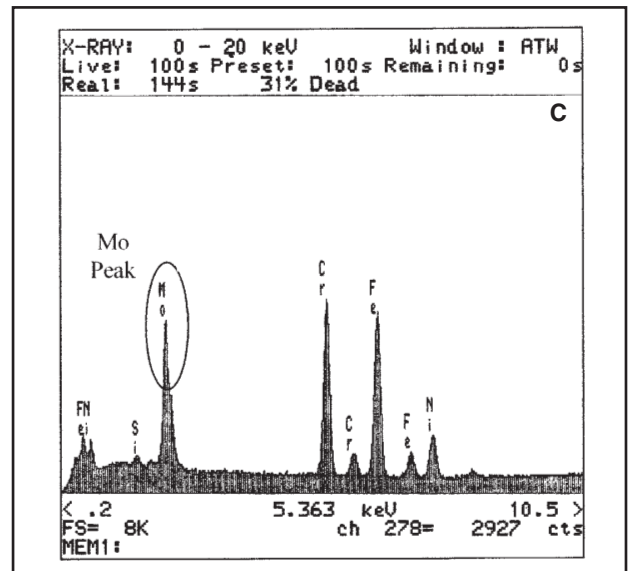
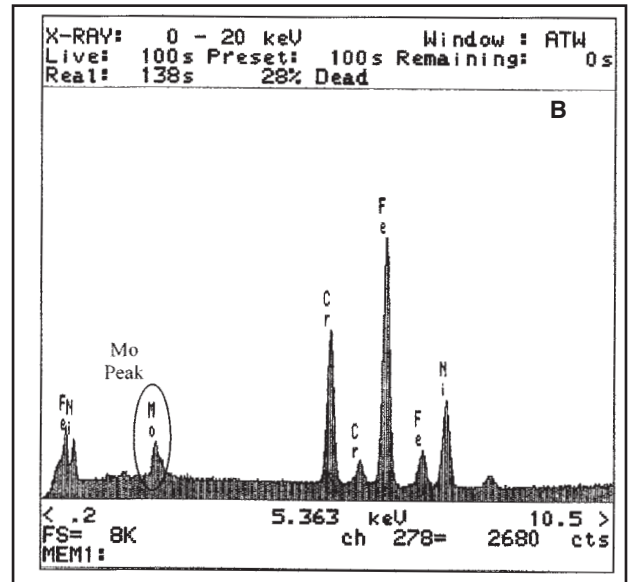
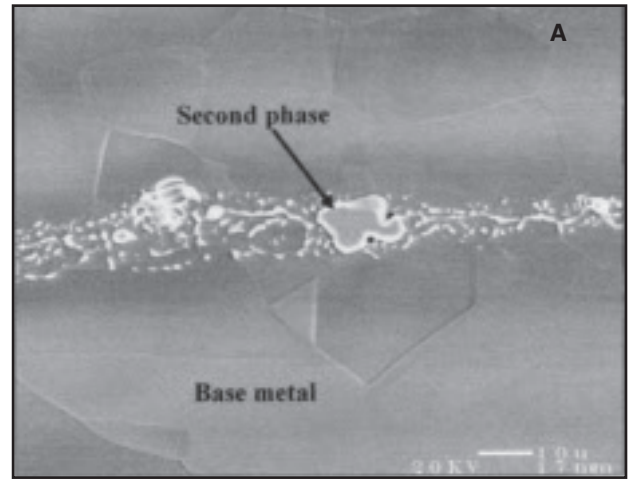


Fig. 2 — A — SEM image of the secondary phase located at midplate thickness in the base metal; B — EDS spectra of the base metal; C — EDS spectra of the second phase.

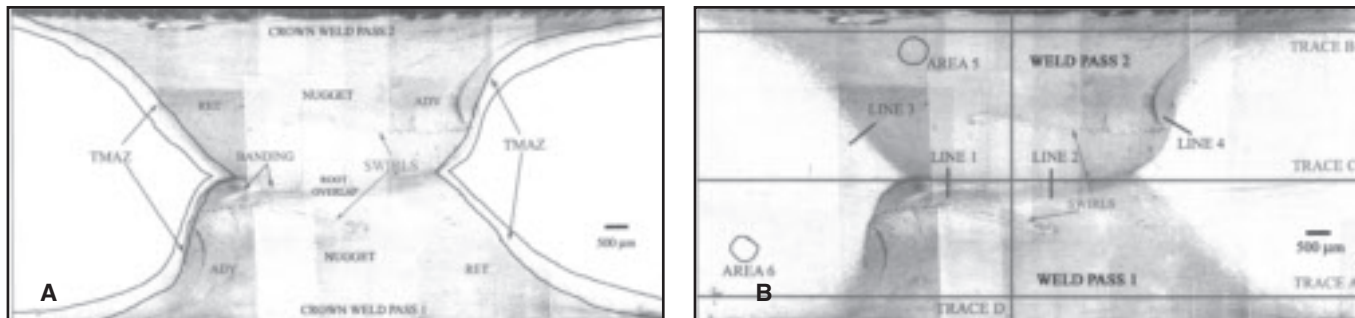


Fig. 3 — Light optical micrograph of a cross-section of the FSW: A — Defining microstructural regions in the weld; B — showing location of microhardness and EPMA traces and several microstructural features.

from the HAZ using a FEI D B235 focused ion beam milling machine and used for preparation of TEM samples. All specimens were prepared across the grain boundaries in the HAZ by milling with a Ga ion beam at an accelerating voltage of 30 kV. To protect the thin section during milling, the surface was covered with a 1-µm-thick Pt layer internally deposited before the milling. After rough sectioning, the specimens were cleaned by a low-dose Ga ion beam (beam current of 300 pA) as the last step to avoid significant Ga contamination. After extracting the specimens from the HAZ, the specimens were mounted on a Cu grid with an amorphous holey carbon film.

Microstructural observation and electron-diffraction analysis of the specimens were both performed in a JEOL JEM-2010F TEM operated at 200 kV. Selected-area diffraction (SAD) was used for phase identification and analysis orientation relationship around grain boundaries in the HAZ. In addition, these regions were also analyzed by energy-dispersive X-ray spectrometry (XEDS) with the incident beam size of ~ 3 nm to support the results of the electron-diffraction analysis.

Results and Discussion

Base Metal Microstructure

The microstructure of the AL-6XN base metal consisted of equiaxed austenite grains with annealing twins — Fig. 1. The average grain size measured approximately $63 \pm 5.6 \mu\text{m}$. This is a typical microstructure for a rolled and annealed superaustenitic stainless steel (SASS). The composition of the base metal was determined using EPMA techniques. As seen in Table 1, the measured composition compares closely to the industrial standard for AL-6XN, with Mo and Ni slightly below the lower limits of the specification.

At higher magnifications, a second phase appearing as streaks was observed near the midplane of the as-rolled plate. A secondary electron SEM image shows this

Table 1 — Composition Analysis of a Doubled-Sided Friction Stir Weld on AL-6XN Obtained Using EPMA

Element	Cr wt %	Mo wt %	Fe wt %	Ni wt %
UNS N08367	20.00–22.00	6.00–7.00	Balance	23.50–25.50
Tolerances				
Base Metal	20.47	5.97	Balance	23.40
Nugget	20.53	5.95	Balance	23.41

phase is different from the rest of the base metal — Fig. 2A. The EDS spectra of both the base metal and second phase are seen in Figs. 2B and C, respectively. Compared to the base metal, the second phase has an increased amount of molybdenum and was previously identified in AL-6XN plate as sigma phase (Refs. 19, 24). Sigma formation is promoted by microsegregation of chromium and molybdenum (Refs. 25, 26) and has been shown to form during solidification of superaustenitic stainless steels (Refs. 26–28). In the case of these AL-6XN plates, sigma likely formed at the centerline of the plate due to segregation during initial solidification of the continuous cast product and persisted during subsequent plate processing. Because sigma is a brittle intermetallic, it can be deleterious to mechanical properties of steel structures and should be avoided (Ref. 29).

Weld Zone Microstructure

Macroscopic views of the double-sided FSW on the AL-6XN plates are seen in Fig. 3A, B. Figure 3A identifies the nugget, the thermal mechanical-affected zone (TMAZ), the retreating (RET) and advancing (ADV) sides of the weld, and some notable features including tungsten swirls (as confirmed later), banding, and the crowns and root overlap of the weld. At the crown (or surface side) of both weld passes, there is a long, shallow region of affected material that is cre-

ated by the pressure of the rotating shoulder against the plate surface during welding (Ref. 30). Below this shallow region, the widths of the first and second pass were approximately 11.5 and 12.7 mm, respectively. At increasing distances from the crown, the weld zone gradually becomes narrower. There is a minimum weld zone thickness of about 6.3 mm near the plate midplane, where the roots (or bottom sides) of the weld passes overlap. A slight asymmetry of each weld pass is seen — the retreating side has a more gradual slope than the advancing side. It is suggested that the asymmetry is created by differences in flow between the advancing and the retreating sides of a FS weld (Ref. 31). On the advancing side, the tool rotation and translation are in the same direction and cause chaotic flow and complex mixing. Flow on the retreating side, however, is generally not as complex — material is simply deformed by tool rotation, but no significant mixing takes place (Refs. 6, 32). Another view of the general shape of the FSW is seen in Fig. 3B. In this figure, the approximate locations of the microhardness traces (Traces A–D) and the approximate lines (Lines 1–4) and areas (Areas 5 and 6) on which EPMA was performed are indicated.

Nugget

As seen in Fig. 3A, the nugget constitutes the majority of the weld affected

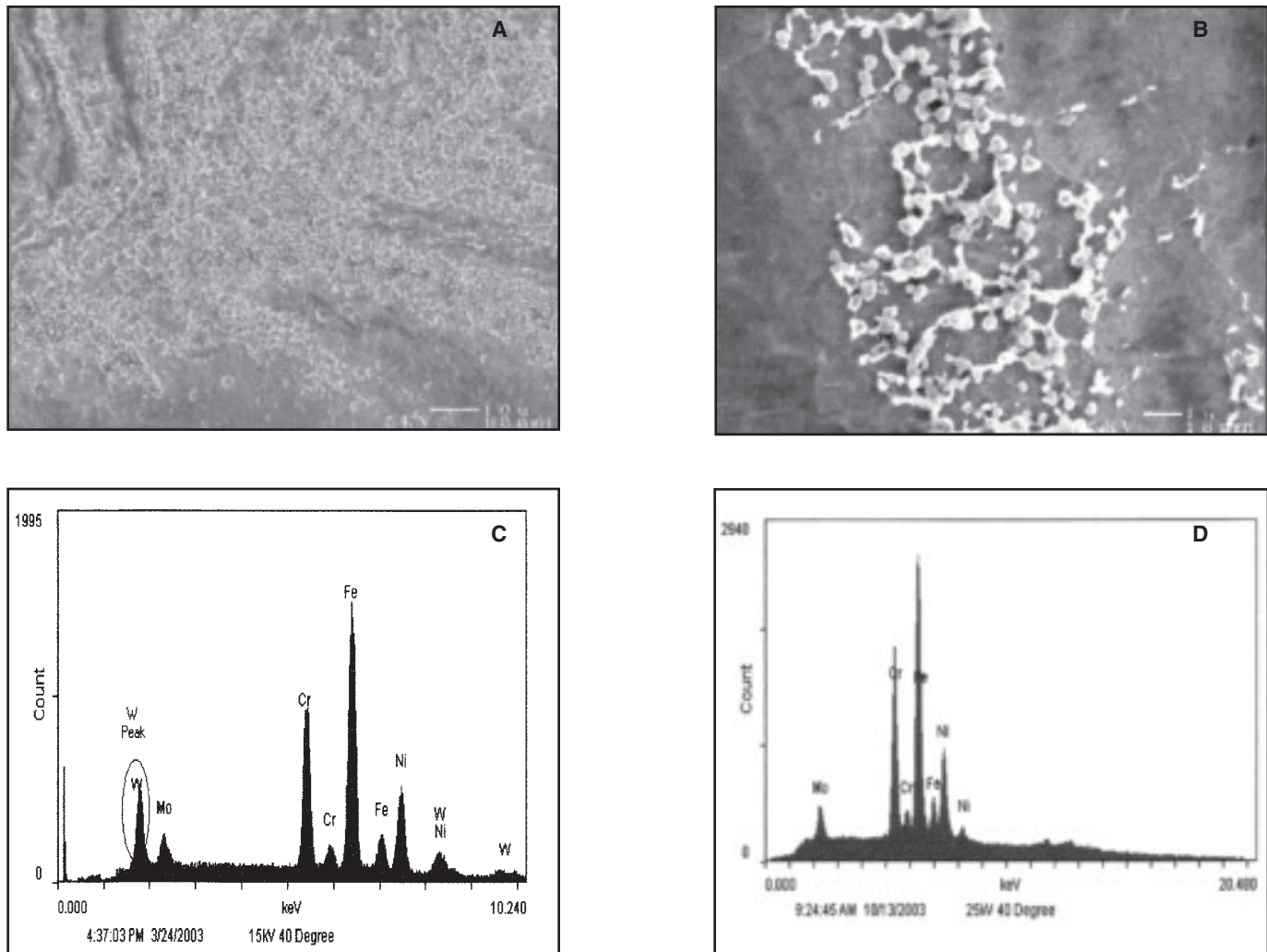


Fig. 4 — A and B are SEM images of the swirl found in the nugget and the EDS spectra obtained from (C) the swirl and (D) the nugget matrix.

zone. No composition change should occur since FSW is an autogenous process requiring no filler metal or flux. The average composition of the nugget, determined by EPMA, was essentially the same as the base metal (Table 1). In general, the microstructure of the nugget consisted of very fine grains not clearly visible using LOM. The nugget grain size was measured at several locations to contrast the $\sim 60\text{-}\mu\text{m}$ sized grains of the base metal. The average grain size near the crown of the weld was approximately $5.9 \pm 0.6 \mu\text{m}$. Near the middle of the nugget, grains were slightly smaller with an average size of $5.1 \pm 0.3 \mu\text{m}$. Grains near the weld roots were the smallest at an average of $4.3 \pm 0.6 \mu\text{m}$. Decreasing grain size from the crown to the root is a trend seen in aluminum alloys as well (Refs. 7, 9). The pressure applied by the tool shoulder results in higher peak temperatures and longer exposure times on the plate surface, allowing for greater grain growth near the surface (Refs. 7, 9). It is important to note that the thermal mechanical cycle of FSW decreases grain size

by an order of magnitude.

Several distinct features are seen in the nugget. Two of the most prominent features are the swirl patterns in each weld that extend from the advancing side of the weld beyond the centerline — Fig. 3A, B. At high magnifications (Fig. 4A, B), it can be seen that the swirls consist of some second phase dispersed in the nugget. Comparing the EDS spectrum from the secondary phase (Fig. 4C) to the nugget EDS spectrum (Fig. 4D), it can be seen that tungsten is detected in the swirl, but is absent in the surrounding material. Although tool wear is not significant during FSW of aluminum alloys, it can be substantial when welding harder materials. For example, during FSW of mild carbon steel using a molybdenum-based tool, wear was shown to result in molybdenum-enriched regions in the weld zone (Ref. 12). In the present case, temperatures and frictional forces are significant enough to cause tool wear, resulting in tungsten contamination in the nugget. There is some evidence that the advancing side may pre-

sent a slightly harsher environment compared to the retreating side. First, the relative velocities of the tool and workpiece are faster on the advancing side. Also, as mentioned previously, material flow is more disruptive on the advancing side because the relative directions of tool rotation and translation. It has also been reported that thermal cycles were more severe on the advancing side than the retreating side (Ref. 33).

There is no appearance of “onion rings” in the nugget as seen in some aluminum alloys (Refs. 9, 10) and 304 stainless steel (Ref. 18), but a “banding” type of phenomenon is seen near the root overlap — Fig. 3A. Figure 5A, a secondary electron SEM image, shows the banding at a higher magnification. In contrast to onion rings in 304 SS FS welds, consisting of alternating layers of ferrite and austenite (Ref. 18), SEM images of the light and dark layers creating the banding in AL-6XN reveal only differences in etching response. The microstructure of the dark layer (Fig. 5B) consists of fine equiaxed grains. However, in an SEM

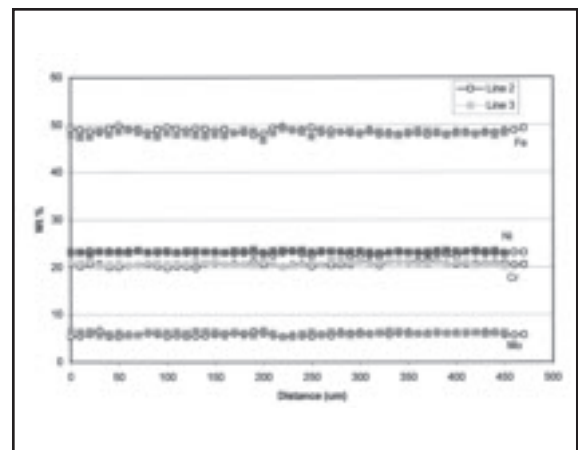
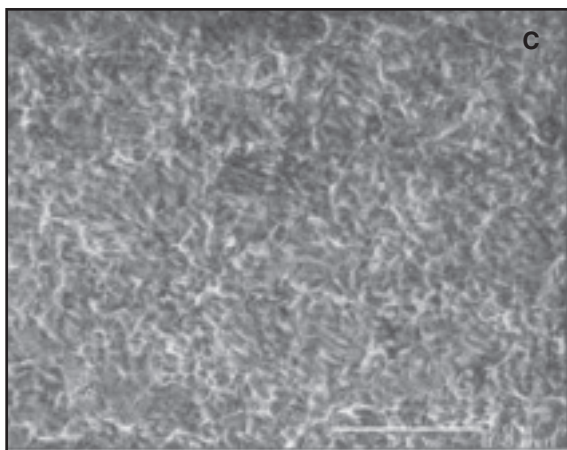
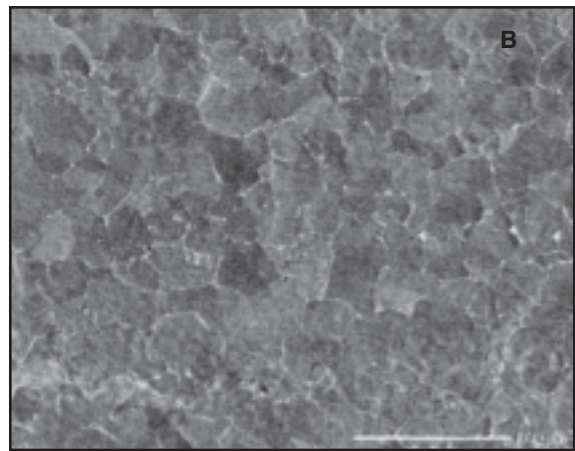


Fig. 5 — A — SEM image of the banding seen at the boundary of weld pass 1 and 2. High magnification SEM images of the (B) dark and (C) light bands seen in A.

Fig. 6 — EPMA data of lines 1 and 2, both of which extend across the boundary of weld pass 1 and 2.

image of the light layer (Fig. 5C), the microstructure is very fine and difficult to resolve. EPMA data of Lines 1 and 2 extend through the banding at the root overlap (Fig. 3B), and a plot of these data (Fig. 6) shows concentration of the elements in this region remained constant. Thus, banding is not the result of composition changes. A possible explanation for the banding is the complex material flow occurring during FSW. When dissimilar metals are joined via FSW, the complex mixing of the two plates is obvious, as etching reveals complex swirls and distinct layers throughout the weld zone (Ref. 2). When two plates of the same material are joined, however, the swirls and vortex patterns are less evident since there are no real composition differences. In this case, the subtle appearance of distinct layers can be the result of variations in deformation regimes (Ref. 34).

Similar to the base metal, a second phase was found near the midplane of the plate in the weld zone — Fig. 7A. EDS analysis of the second phase (Fig. 7B) again detects an increased concentration

of molybdenum compared to the base metal (Fig. 2B). Some of the second phase was also found near the edge of the nugget bordering the TMAZ — Fig. 7C. Only a few, isolated fragments of sigma were seen in the nugget in contrast to the base metal. Before welding, the morphology of the sigma in this region most likely appeared similar to the centerline sigma in the base metal. The intense deformation and complex material flow during welding, however, caused the sigma to be re-distributed away from the midplane. It is likely that more sigma is distributed throughout the nugget, but is very fine and was undetected with the LOM or SEM magnifications used in this study. It should be stressed that the sigma phase found in the nugget originated in the base metal and thus existed prior to the welding process. Nevertheless, from Fig. 6, it is seen that microsegregation, which promotes sigma formation during solidification of fusion welds, has been avoided. Thus, it is unlikely that sigma would form during FSW.

Heat-Affected Zone and Thermal Mechanical-Affected Zone

As mentioned previously, the TMAZ surrounds the nugget and the HAZ surrounds the TMAZ. The HAZ consists of the same large equiaxed austenite grains seen in Fig. 1 of the base metal. Having experienced only the thermal cycles of FSW, grain growth in the HAZ might be expected but is not evident. The difference between the base metal and the HAZ is very subtle and defining the exact boundary between the two is difficult. The only distinguishing feature between the two regions is the presence of a fine phase at the grain boundaries in the HAZ — Fig. 8. Posada et al. noted the same phenomenon in Al-6XN FS welds and suggests that it is either recrystallized grains or precipitated sigma phase (Ref. 19).

A TEM photomicrograph of the microstructure around a grain boundary in the HAZ is shown in Fig. 9. This image shows two original austenite grain boundaries (indicated by several arrows) and the small

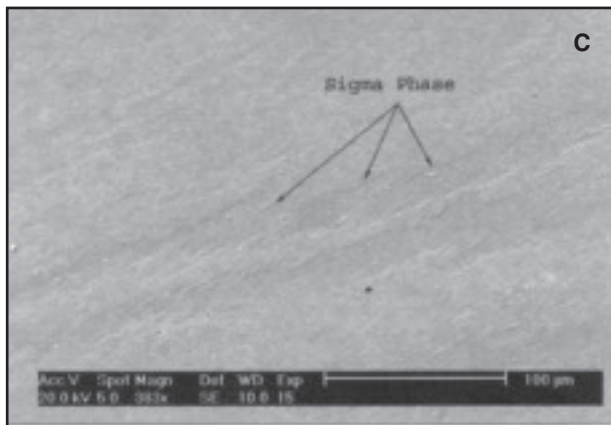
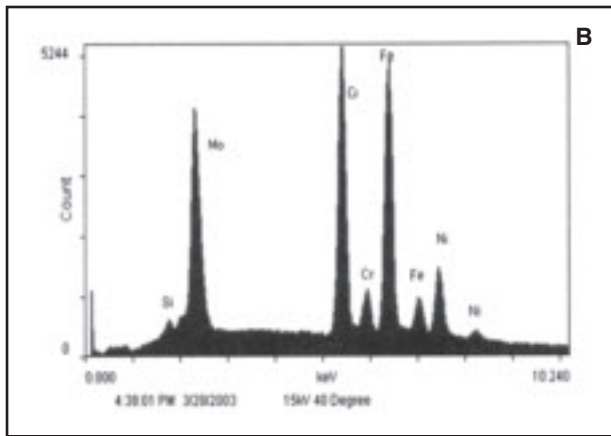
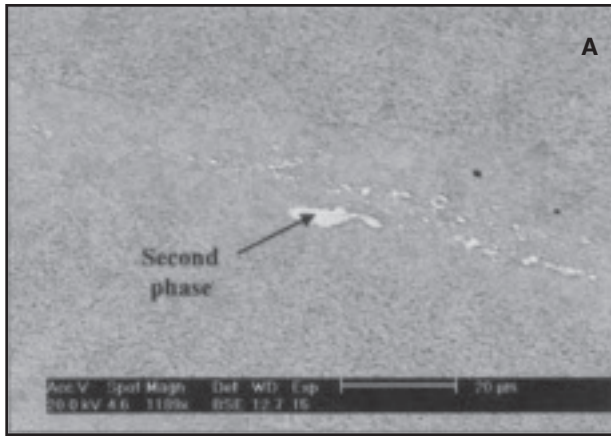


Fig. 7 — A — SEM image of the secondary phase in the nugget similar to the sigma phase in the base metal; B — the EDS spectrum of that phase; C — additional sigma located throughout the nugget.

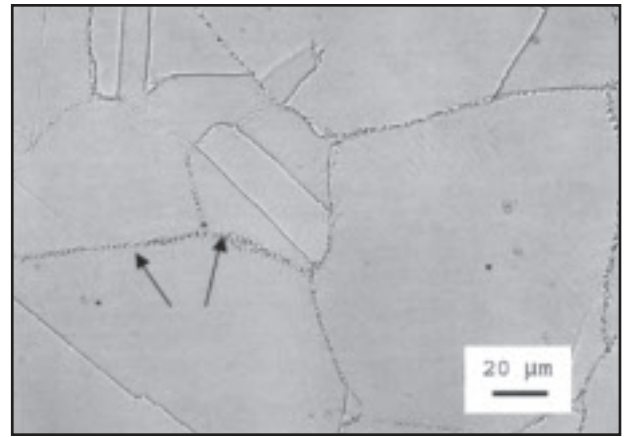


Fig. 8 — Light optical micrograph showing smaller grains located at the grain boundaries of the HAZ.

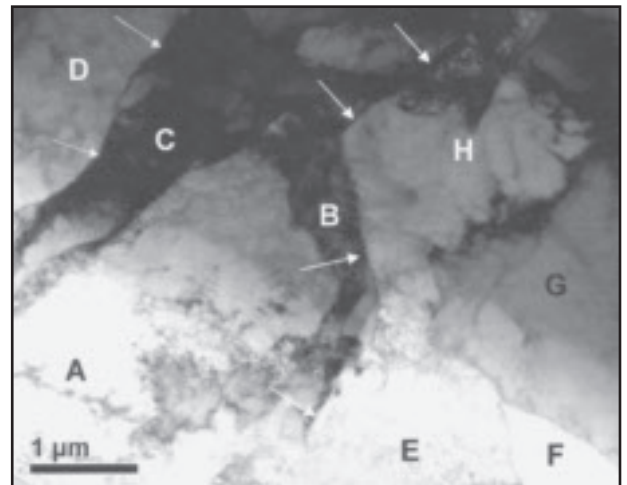


Fig. 9 — Microstructure at the original austenite grain boundaries of the HAZ.

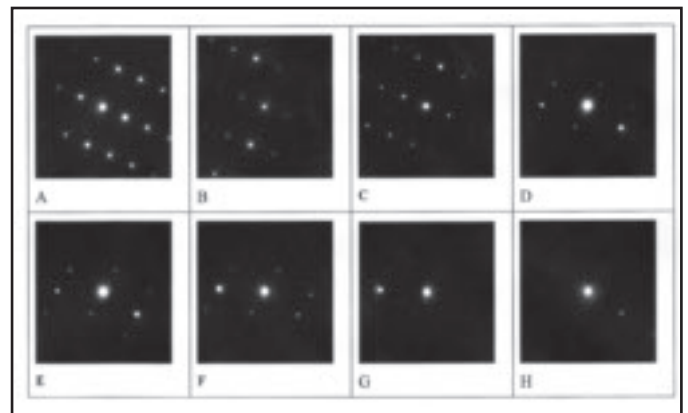


Fig. 10 — A–F — SAD patterns obtained from regions labeled A–H.

features decorating the boundary (indicated by letters). The SAD patterns from the indicated features were obtained for phase identification and to determine their orientation relationship — Fig. 10A–H.

The SAD pattern at region A was typical for an FCC metal oriented along the (112) plane — Fig. 10A. Regions B and C produced similar SAD patterns with slight

orientation differences — Fig. 10B, C. Therefore, regions identified as A–C are subgrains, separated by only low angle grain boundaries. On the opposite side of the grain boundary, regions E–H have a similar orientation to one another (Fig. 10E–H), but are different than regions A–D. Again, regions E–H differ in orientation by a small angle and are subgrains. Although these

subgrains are not oriented along a major zone axis, the crystal structure is still revealed. The diffraction patterns of Fig. 10E–H are also of an FCC structure, not the tetragonal crystal structure of sigma. Region D has a similar pattern to regions E–H and probably constitutes another FCC grain separated from subgrains A–C by a grain boundary. This phenomenon was also

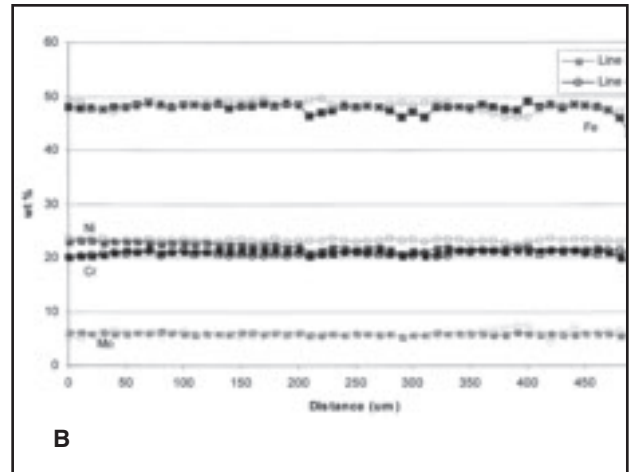
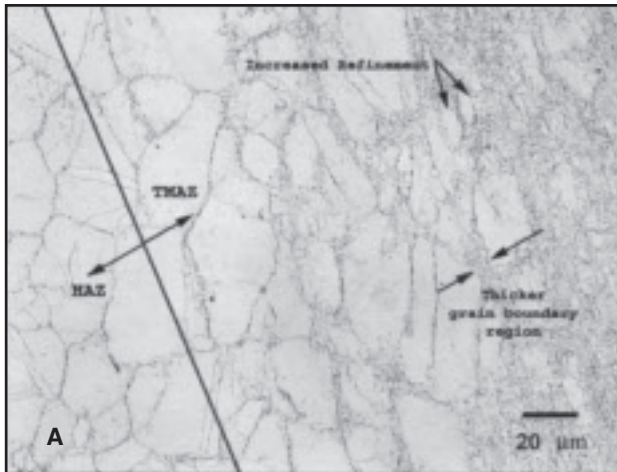


Fig. 11 — A — Light optical image of the TMAZ where a transition from a pure HAZ microstructure to a nugget type of microstructure is seen. B — the EPMA data of Lines 3 and 4, both of which extend through the different microstructural regions of the FSW.

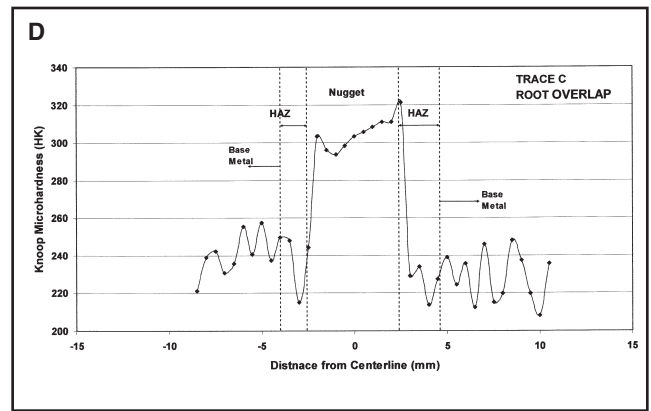
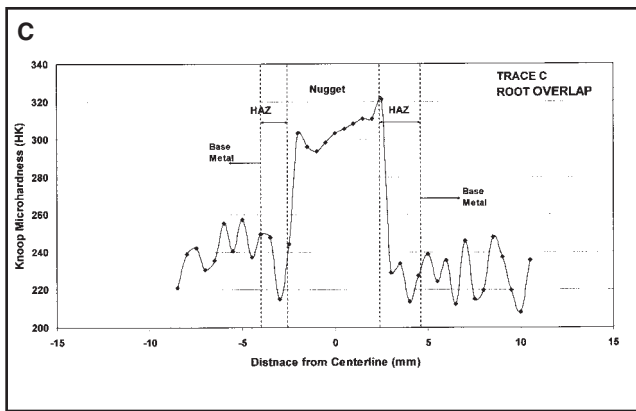
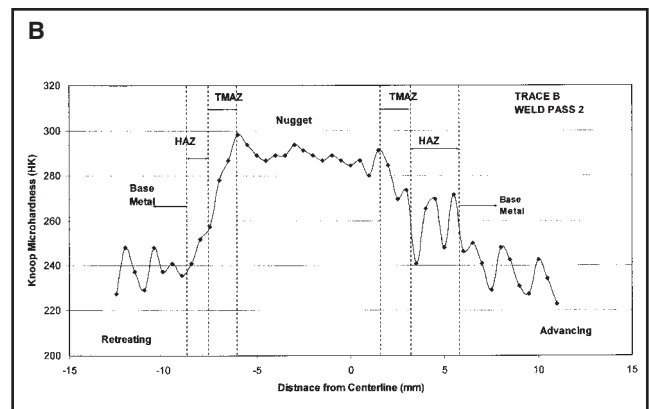
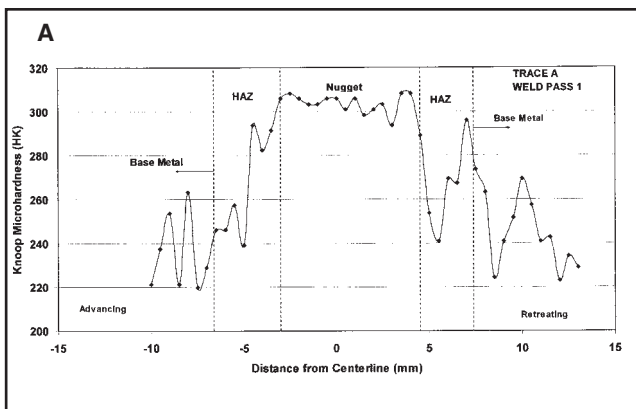


Fig. 12 — Microhardness traces as a function of distance: A — From the centerline across weld pass 1; B — from the centerline across weld pass 2; C — from the centerline across the weld pass overlap; and D — from the plate mid-plane along the weld centerline.

investigated at another site in the HAZ and similar results were found. From the TEM analysis, it can be said that the fine grains found in the prior austenite grain boundaries in the HAZ are due to austenite recrystallization at these sites and not the formation of sigma phase.

The exact source of the deformation required to cause this recrystallization at the grain boundaries is not clear. One possibility is that the combination of residual

stress from plate processing and the specific time and temperature environment produced during FSW promoted recrystallization of austenite. It is also possible that, although this microstructure was referred to as the HAZ (implying that only temperature cycles affected the microstructure), strain may have reached the critical minimum to induce recrystallization.

The microstructure of the TMAZ is best described as a transition region from

a complete HAZ microstructure to a complete nugget type of microstructure — Fig. 11A. The transition is a result of decreasing strain and strain rates and milder thermal cycles with increasing distance from the centerline. Because the changes from the TMAZ and HAZ zone are so gradual, the line drawn in Fig. 11A defines only an approximate HAZ/TMAZ boundary. Near this boundary, microstructural changes of the TMAZ are mainly the re-

sult of thermal cycles — evidence that deformation is minimal here. Moving toward the right in the figure, strain caused by tool rotation begins to dominate the microstructural changes, leading to a more refined structure. As seen in Fig. 11A, higher strains deform the original austenite more severely and promote more recrystallization at the original austenite grain boundaries. Adjacent to the weld nugget, most of the TMAZ appears completely refined, but several larger austenite grains persist.

In addition, EPMA data along Lines 3 and 4 (Fig. 3B) provided a composition analysis of the different microstructural regions. The data showed no variation in elemental concentration with distance (Fig. 11B), and appeared essentially the same as data obtained from Lines 1 and 2 (Fig. 6). From all EPMA traces, it can be concluded there is no form of segregation in the AL-6XN welds.

Microhardness

The average microhardness of the base metal was measured at approximately 243 ± 9 HK. Four microhardness traces were performed across the welded region (Fig. 3B). Figure 12A–C shows plots of microhardness as a function of distance from the centerline for traces A, B, and C, respectively. As labeled on the figures, changes in microhardness are correlated to the microstructural transition from the base metal to the nugget. In all plots, hardness is highest in the fine-grained nugget region. All microstructural zones are represented in trace B — Fig. 12B. Since the TMAZ is narrow, no data points fell within this region for trace A (Fig. 12A) and trace C (Fig. 12C). Despite this, it can clearly be seen that hardness decreases with increasing distance from the weld centerline. As mentioned above, the TMAZ consists of a mix of deformed austenite grains and small grains at grain boundaries. In general, this microstructure yields hardness values similar to, but slightly lower than, the nugget. The large austenite grains and smaller grains of the HAZ yield a range of hardness values between the TMAZ and base metal hardness. The TMAZ and HAZ, both transition zones separating the nugget and the base metal, show a trend of decreasing hardness moving away from the nugget. These zones also exhibit considerable scatter in the data — a result of the nature of the microstructure and of microhardness testing.

Trace D was taken through the plate thickness near the weld centerline (Fig. 3B). Figure 12D shows a plot of microhardness measurements as a function of distance from the midplane of the plate. The two maximum data points correspond to the microhardness of the tungsten swirls in the microstructure.

Conclusions

The resulting microstructure of a double-sided FSW on AL-6XN plate was examined using LOM, SEM, TEM, and microhardness techniques. Significant results of the study are as follows:

1. The intense deformation and temperatures experienced by the nugget produce a very fine microstructure of equiaxed grains.

2. Evident from the stream of tungsten contamination found in the microstructure, tool wear proves to be a significant problem in FSW of AL-6XN with the current tool material. The wear debris was predominately observed on the advancing side of the weld.

3. As expected, there was no evidence of segregation in any region of the weld, which is significantly different than conventional fusion welding where microsegregation is an unavoidable occurrence when joining SASS.

4. The HAZ and the TMAZ are transition zones between the base metal and the nugget. The HAZ microstructure is characterized by large austenite grains similar to the base metal with recrystallization of austenite at grain boundaries. No evidence of sigma phase at the austenite grain boundaries was found. There are no apparent signs of deformation in this region. The TMAZ is simply a microstructural transition from the HAZ to the nugget. Approaching the weld centerline, effects of the increasing strains and higher temperatures produced during FSW are seen by the increased grain deformation and recrystallization at grain boundaries.

5. Microhardness traces reflect the microstructural changes in the different regions created during FSW. Generally, the base metal is softer than any weld-affected region. Hardness increases toward the centerline, through the HAZ and TMAZ, as a result of increasing microstructural refinement. The fine-grained structure of the nugget yields maximum hardness.

Acknowledgments

The authors gratefully acknowledge the financial support for this work provided by the Office of Naval Research (ONR). Masashi Watanabe provided the TEM characterization. Discussions with Matthew J. Perricone and Shane A. Para are also greatly appreciated.

References

1. Thomas, W. M., Nicholas, E. D., Needham, J. C., Murch, M. G., Temple-Smith, P., and Dawes, C. J. 1991. Friction Stir Butt Welding. U.S. Patent No. 5,460,317.
2. Li, Y., Murr, L. E., and McClure, J. C. 1999. Flow visualization and residual microstructures associated with the friction-stir

welding of 2024 aluminum to 6061 aluminum. *Materials Science & Engineering A* 271: 213–223.

3. Reynolds, A. P., Lockwood, W. D., and Seidel, T. U. 2000. Processing-property correlation in friction stir welds. *Materials Science Forum* 331–337: 1719–1724.

4. Heinz, B., Skrotzki, B., and Eggeler, G. 2000. Microstructural and mechanical characterization of a friction stir welded Al-alloy. *Materials Science Forum* 331–337: 1757–1762.

5. Nicholas, E. D., and Thomas, W. M. 1998. A review of friction processes for aerospace applications. *International Journal of Materials and Product Technology* 13: 45–55.

6. Reynolds, A. P. 2000. Visualisation of material flow in autogenous friction stir welds. *Science and Technology of Welding and Joining* 5: 120–124.

7. Norman, A. F., Brough, I., and Prangnell, P. B. 2000. High resolution EBSD analysis of the grain structure in an AA2024 friction stir weld. *Materials Science Forum* 331–337: 1713–1718.

8. Rhodes, C. G., Mahoney, M. W., Bingel, W. H., Spurling, R. A., and Bampton, C. C. 1997. Effects of friction stir welding on microstructure of 7075 aluminum. *Scripta Materialia* 36: 69–75.

9. Sutton, M. A., Yang, B., Reynolds, A., and Taylor, R. 2002. Microstructural studies of friction stir weld in 2024-T3 aluminum. *Materials Science & Engineering A* A323: 160–166.

10. Krishnan, K. N. 2001. On the formation of onion rings in friction stir welds. *Materials Science & Engineering A* A327: 246–251.

11. Stoltz, S. 2000. The What, Where and How of Friction Stir Welding. II: 469–472. ET 2000: Seventh International Aluminum Extrusion Technology Seminar.

12. Lienert, T. J., Jr., Stellwag, W. L., Grimmett, B. B., and Warke, R. W. 2003. Friction stir welding studies on mild steel. *Welding Journal* 82(1): 1-s to 9-s.

13. Woo, I., Aritoshi, M., and Kikuchi, Y. 2002. Metallurgical and mechanical properties of high nitrogen austenitic stainless steel friction welds. *ISIJ International* 42: 401–406.

14. Garner, A. Pitting corrosion of high alloy stainless steel weldments in oxidizing environments. 1983. *Welding Journal* 62(2): 27–34.

15. Banovic, S. W., DuPont, J. N., and Marder, A. R. 2002. Dilution and microsegregation in dissimilar metal welds between super austenitic stainless steel and nickel base alloys. *Science and Technology of Welding and Joining* 7: 374–383.

16. Tuthill, A. H., and Avery, R. E. 1993. Corrosion behavior of stainless steel and high-alloy weldments in aggressive oxidizing environments. *Welding Journal* 72(2): 41-s to 49-s.

17. Reynolds, A. P., Tang, W., Gnaupel-Herold, T., and Prask, H. 2003. Structure, properties, and residual stress of 304L stainless steel friction stir welds. *Scripta Materialia* 48: 1289–1294.

18. Posada, M., DeLoach, J., Reynolds, A. P., Skinner, M., and Halpin, J. P. 2001. Friction stir weld evaluation of DH-36 and stainless steel weldments. *Friction Stir Welding and Processing*, pp. 159–171.

19. Posada, M., DeLoach, J., Reynolds, A. P., and Halpin, J. 2003. Mechanical property and microstructural evaluation of friction stir welded AL-6XN. *Proceedings of the 6th International Trends in Welding Research Conference*,

pp. 307–311.

20. ASTM E112-95, *Standard Test for Determining Grain Size*. 1995. Conshohocken, Pa.: American Society for Testing and Materials.

21. ASTM E384, *Standard Test Method for Microhardness of Materials*. 1989. Conshohocken, Pa.: American Society for Testing and Materials.

22. DuPont, J. N., Robino, C. V., and Marder, A. R. 1998. Modeling solute redistribution and microstructural development in fusion welds of Nb-bearing superalloys. *Acta Mater* 46: 4781–4790.

23. Heinrich, K. F. J., Romig Jr., A. D., and Chambers, W. F. 1986. *Microbeam Analysis* 21: 279–280.

24. Friedersdorf, L. E., and Luer, K. Susceptibility of AL-6XN gas tungsten arc weldments to localized corrosion. *Atlss Report No. 03-09, 1-44*. 2003. Bethlehem, Pa.: Atlss.

25. Ogawa, T., and Koseki, T. 1996. *Welding*

high-molybdenum superaustenitic stainless steel. *Materials Selection & Design* 87–91.

26. Dixon, B., Calleja, P., Jackson, I., Russell, J., Ryan, G., Gunner, A., and Lynch, S. 1999. Low ductility fracture of welded superaustenitic UNS S31245 stainless steel. *ASM International. Trends in Welding Research*. pp. 865–869.

27. Sedriks, A. J. 1989. New stainless steels for seawater service. *Corrosion*.

28. Avesta Stainless Steels, Information Brochure no. 7945. 1979. Sweden, Avesta Jernverks.

29. Finlay, M. R., and Orszag, F. 1997. Sigma phase embrittlement of 304H austenitic stainless steel. New York, N.Y.: ASME. ASME Pressure Vessels and Piping Conference. pp. 253–260.

30. Thomas, W. M., Threadgill, P. L., and Nicholas, E. D. 1999. Feasibility of friction stir welding steel. *Science and Technology of Weld-*

ing and Joining 4: 365–372.

31. Kwon, Y. J., Saito, N., and Shigematsu, I. 2002. Friction stir process as a new manufacturing technique of ultrafine grained aluminum alloy. *Journal of Materials Science Letters* 21: 1473–1476.

32. Colligan, K. 1999. Material flow behavior during friction stir welding of aluminum. *Welding Journal* 78(7): 229-s to 237-s.

33. Mishra, R. S., Sharma, S. R., Mara, N. A., and Mahoney, M. W. 2000. Mechanical properties of friction stir welded aluminum alloys. *Joining of Advanced and Specialty Materials*, pp. 157–159.

34. Prado, R. A., Murr, L. E., Shindo, D. J., and Soto, K. F. 2001. Tool wear in the friction stir welding of aluminum alloy 6061 + 20% Al₂O₃: A preliminary study. *Scripta Materialia* 45: 75–80.

Correction

In the welding research paper that ran on pages 41-s to 51-s of the March 2005 *Welding Journal* titled “Processing of Alumina-Niobium Interfaces via Liquid-Film-Assisted Joining,” each instance in which the symbol \oplus appears should have been an approximately equal to sign (\approx). For example, the abstract should have read as follows:

“Alumina-niobium interfaces were fabricated at 1400°C via solid-state diffusion brazing of a 127- μ m-thick niobium foil between alumina blocks. Prior to brazing, some of the alumina mating surfaces, both polished and unpolished, were evaporation-coated with copper films ≈ 1.4 , ≈ 3.0 , and ≈ 5.5 μ m thick to induce liquid-film-assisted joining at the brazing

temperature. The effects of copper film thickness and surface roughness on fracture characteristics and ceramic-metal interfacial microstructure were investigated by room-temperature four-point bend tests, optical microscopy, profilometry, and atomic force microscopy. The average strength of bonds between niobium and polished alumina substrates increased with the introduction of copper film interlayers, and the scatter in strength tended to decrease, with an optimum combination of strength and Weibull modulus arising for a copper film thickness of 3.0 μ m. The strength characteristics of niobium bonded to unpolished alumina substrates were also improved by liquid-film-assisted joining, but were unaffected by the thickness of the copper interlayers.”

The incorrect signs also appeared on pages 42-s through 49-s.

In addition, two less than or equal to signs (\leq) appeared as quotation marks. The last two sentences in the first column of page 43-s should have read as follows:

“Increasing alumina roughness resulted in a modest ($\leq 10\%$) decrease in average strength, increased scatter in strength, and a decrease in the area fraction of alumina-niobium contact (98% \rightarrow $\approx 80\%$). In contrast, increasing niobium roughness resulted in a modest ($\leq 10\%$) increase in average strength, and an increase in the area fraction of alumina-niobium contact ($\approx 80\%$ \rightarrow $\geq 99\%$).”

The *Welding Journal* apologizes for the errors.

Call for Papers

The American Welding Society announces a Call for Papers for the Professional Program that will be a part of the first-ever alliance of the AWS Welding Show and FABTECH International. This premier event will be held November 13–16, 2005, at McCormick Place in Chicago, Illinois.

Submissions should fall in one of the following three categories and will be accepted only in a specific format. Individuals interested in participating should contact Tom Davis, Operations Manager, via email at tdavis@aws.org for specific details. Deadline for submission of papers is Friday, May 20, 2005.

Technical/Research Oriented

- New science or research.
- Selection based on technical merit.
- Emphasis is on previously unpublished work in science or engineering relevant to welding, joining, and allied processes.
- Preference will be given to submittals with clearly communicated benefit to the welding industry.

Applied Technology

- New or unique applications.
- Selection based on technical merit.
- Emphasis is on previously unpublished work that applies known principles of joining science or engineering in unique ways.
- Preference will be given to submittals with clearly communicated benefit to the welding industry.

Education

- Welding education at all levels.
- Emphasis is on education/training methods and their successes.
- Papers should address overall relevance to the welding industry.

The essential standard for quality fabrication.

Now available in Structural Bundles that save you money too.

AWS D1.1, *Structural Welding Code—Steel*

Save time and money, and maximize reliability and safety, with the 2004 edition of AWS D1.1, *Structural Welding Code—Steel*. Engineers, architects, and fabricators depend on this book to ensure the integrity of welded steel structures. ANSI Approved.

AVAILABLE AS A CD TOO!

New for 2004:

- Contains the latest workmanship standards, inspection procedures, acceptance criteria
- Clarifies requirements that need an engineer's approval, minimizing code-interpretation conflicts
- Modifies allowable stress range formulae
- Enhances construction integrity safety by requiring additional tests when FCAW and GMAW constant current power supplies are used
- Reflects advances in technology by the addition of new steels to pre-qualified base metal list
- Adjusts welder qualification essential variables
- Adjusts dimensions and tolerances on prequalification joint details



Order today. Call us at 800.854.7179 or visit global.ihs.com to get your copy.

D1.1/D1.1M:2004, *Structural Welding Code—Steel*

Order Code: AWS D1.1/D1.1M, Nonmembers: \$360, AWS Members: \$270

D1.1/D1.1M:2004 CD, *Structural Welding Code—Steel*

Order Code: AWS D1.1/D1.1M CD, Nonmembers: \$380, AWS Members: \$285

D1.1/D1.1M:2004 COMBO, *Structural Welding Code—Steel*

Order Code: AWS D1.1/D1.1M COMBO, Nonmembers: \$620, AWS Members: \$465

Save \$\$\$ with these AWS Structural Bundles

CODE	YEAR	TITLE	INDIVIDUAL PRICING NONMEMBER	INDIVIDUAL PRICING MEMBER	BUNDLE PRICE 15% OFF NONMEMBER	BUNDLE PRICE 15% OFF MEMBER
Bundle A - Structural Steel/AISC Steel Building Structures						
AWS D1.1/D1.1M	2004	STRUCTURAL WELDING CODE—STEEL	\$360	\$270		
AWS A2.4	1998	STANDARD SYMBOLS FOR WELDING, BRAZING, AND NONDESTRUCTIVE EXAMINATION	\$136	\$102		
AWS A3.0	2001	STANDARD WELDING TERMS AND DEFINITIONS	\$128	\$96		
Bundle Total			\$624	\$468	\$532	\$399
Bundle B - D1 All Structural Welding Codes						
AWS D1.1/D1.1M	2004	STRUCTURAL WELDING CODE—STEEL	\$360	\$270		
AWS D1.2/D1.2M	2003	STRUCTURAL WELDING CODE—ALUMINUM	\$132	\$99		
AWS D1.3	1998	STRUCTURAL WELDING CODE—SHEET STEEL	\$100	\$75		
AWS D1.4	1998	STRUCTURAL WELDING CODE—REINFORCING STEEL	\$84	\$63		
AASHTO/ AWS D1.5M/D1.5	2002	BRIDGE WELDING CODE	\$188	\$141		
AWS D1.6	1999	STRUCTURAL WELDING CODE—STAINLESS STEEL	\$132	\$99		
Bundle Total			\$996	\$747	\$848	\$636
Bundle C - AISC Conventional and Complex Steel Building Structures						
AWS D1.1/D1.1M	2004	STRUCTURAL WELDING CODE—STEEL	\$360	\$270		
AWS A2.4	1998	STANDARD SYMBOLS FOR WELDING, BRAZING, AND NONDESTRUCTIVE EXAMINATION	\$136	\$102		
Bundle Total			\$496	\$372	\$424	\$318
Bundle D - AISC Simple and Major Steel Bridges						
AASHTO/ AWS D1.5M/D1.5	2002	BRIDGE WELDING CODE	\$188	\$141		
AWS A2.4	1998	STANDARD SYMBOLS FOR WELDING, BRAZING, AND NONDESTRUCTIVE EXAMINATION	\$136	\$102		
Bundle Total			\$324	\$243	\$276	\$207
Bundle E - Structural Aluminum						
AWS D1.2/D1.2M	2003	STRUCTURAL WELDING CODE—ALUMINUM	\$132	\$99		
AWS A2.4	1998	STANDARD SYMBOLS FOR WELDING, BRAZING, AND NONDESTRUCTIVE EXAMINATION	\$136	\$102		
AWS A3.0	2001	STANDARD WELDING TERMS AND DEFINITIONS	\$128	\$96		
Bundle Total			\$396	\$297	\$336	\$252



American Welding Society

Visit our Web site www.aws.org
for membership information

Circle No. 31 on Reader Info-Card